Chapter 2
Gyroid and Gyroid-Like Surfaces

This chapter gives an overview of the fascinating gyroid and gyroid-like surfaces, which are found in nature as intermaterial dividing surfaces. The single- and double-gyroid surfaces in particular will be discussed. In order to visualize these gyroidal structures the concept of a level surface will be introduced and applied.

2.1 Intermaterial Dividing Surfaces

The immiscible components of block copolymers separate into distinct domains on the microscale in response to thermodynamic driving forces, that will be discussed in Chap. 4. The interfaces separating these domains have approximately constant mean curvature

$$H = \frac{1}{2}(k_1 + k_2) = \text{const.}, \tag{2.1}$$

where k_1 and k_2 are the principal curvatures. These surfaces are called intermaterial dividing surfaces (IMDS). Beside a number of unconnected periodic arranged IMDSs (e.g. spheres, lamellae and cylinders), multicontinuous triply periodic surfaces exist which are of particular interest, see Chap. 1. A bicontinuous (tricontinuous) triply periodic IMDS separates space into two (three) regions, forming connected networks which are periodic in three independent directions, such as the double primitive structure, discovered in a polymer/ceramic precursor composite [2, 3]. However, some of these structures were reevaluated as deformed double-gyroids [4]. The only bicontinuous IMDS in the phase diagram of pure diblock copolymers is the orthorhombic *Fddd* network and the only tricontinuous is the double-gyroid [5]. Copolymers containing more than two chemically distinct and incompatible block materials can adopt morphologies with more than three continuous phases, including the pentacontinuous core-shell double-gyroid discovered in ABC triblock copolymers [6, 7]. In other

Parts of this chapter are taken from my master's thesis [1].

M. R. J. Scherer, *Double-Gyroid-Structured Functional Materials*,
Springer Theses, DOI: 10.1007/978-3-319-00354-2_2,

self-organizing systems the bicontinuous single-gyroid microdomain structure can be found. Cubic phases with space group symmetry $I4_132$ (double-gyroid) and $Im\bar{3}m$ (double primitive) have also been identified in thermotropic liquid crystals [8].

All IMDSs can be approximated by constant mean curvature (CMC) surfaces that minimize interfacial area subject to a volume (or volume fraction) constraint. This fact is not surprising, since the microdomain structure is the result of the balance between chain-stretching and the interfacial energies, where the latter term seeks to minimize surface area and thus favors CMC surfaces.

Since analytical expressions for only a few continuous triply periodic CMC surfaces are known (e.g. the Enneper-Weierstrass parameterization of the single-gyroid minimal surface with $H = 0$ and a volume fraction of 50 % [9]), these surfaces are typically modeled with the help of level surfaces.

2.2 Level Surfaces

Level surfaces are represented by functions $F : \mathbb{R}^3 \to \mathbb{R}$ of points $(x, y, z) \in \mathbb{R}^3$, which satisfy the equation

$$F(x, y, z) = t, \tag{2.2}$$

where t is a constant [10]. The form of the surface is controlled by $F(x, y, z)$, while the parameter t determines the volume fraction of the regions that are separated by the surface.

Level surfaces of all IMDSs are defined by

$$F(x, y, z) = \sum_{hkl} |F(hkl)| \cdot \cos\left(\frac{2\pi}{L}(hx + ky + lz) - \alpha_{\text{hkl}}\right), \tag{2.3}$$

where $F(hkl)$ denotes the structure factor amplitude, reflecting the symmetry of the structure, α_{hkl} the phase angle and L the cubic unit cell edge length [11]. The set of allowed hkl values of the Fourier components of the structure and the Fourier series representation of the space group can be found in the *International tables of X-ray crystallography*. It was found that the generated level surface is virtually independent of the number of coefficients of the Fourier series, thus taking only the lower orders hkl values into account provides a sufficiently close approximation to the true CMC surface [11].

2.3 Single-Gyroid

The single-gyroid (SG) IMDS with $I4_132$ (No. 214) symmetry was first discovered in 1967 by Luzzati et al. as a cubic phase occurring in strontium soap surfactants and in pure lipid-water systems [12, 13]. In 1970, Schoen identified the minimal

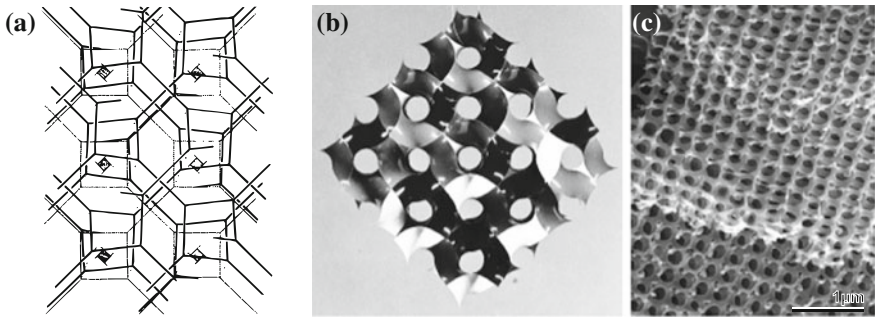

Fig. 2.1 The single-gyroid or Schoen G surface. **a** Drawing by Luzzati et al. from 1970 showing the two mutually interwoven networks separated by the G surface (Reprinted by permission from Macmillan Publishers Ltd: Nature, Luzzati et al. [12], Copyright 2013). **b** Plastic model of the gyroid minimal surface by Schoen from 1970 (Reprinted from [14]). **c** Scanning electron micrograph showing the porous cuticular single-gyroid of a *Callophrys rubi* wing scale. (Reprinted from Schröder-Turk et al. [18], Copyright 2013, with permission from Elsevier)

gyroid, therefore also called the Schoen G surface, as one of a further 17 examples of intersection-free triply periodic minimal surfaces (TPMS), in addition to the five cases already known, and gave a mathematical description [14].

The SG IMDS has been discovered in the cuticular structure of butterfly wing scales [15, 16]. The structure is made of chitin and air serving as biological photonic crystal to produce beautiful iridescent colors [16–18]. More recently, the mitochondria located at the inner segment of the retinal cones of tree shrew was found to contain a multi-layer gyroid membrane arrangement similar to the SG structures observed in butterflies. The highly order structure is believed to potentially function either as a multi-focal lens, as an angle-independent interference ultraviolet filter, or as a waveguide photonic crystal [19] (Fig. 2.1).

The single-gyroid of constant mean curvature can be approximated by a level surface. Although this approach does not result in CMC surfaces, it is extremely useful for simulations. Inserting the lowest allowed hkl values of the $I4_132$ space group ($|F(110)| = |F(\bar{1}10)| = 1$ and $\alpha(110) = \alpha(\bar{1}10) = \pi/2$) in Eq. (2.3) provides an unique equation for the single-gyroid level surface [11, 20]

$$F_{SG}(x, y, z) = t \tag{2.4}$$

$$\sin\left(\frac{2\pi}{L}x\right)\cos\left(\frac{2\pi}{L}y\right) + \sin\left(\frac{2\pi}{L}y\right)\cos\left(\frac{2\pi}{L}z\right) + \sin\left(\frac{2\pi}{L}z\right)\cos\left(\frac{2\pi}{L}x\right) = t, \tag{2.5}$$

where L is the cubic unit cell length.

The possible values for t and the resulting structures are discussed below:

- $t = 0$:
  The resulting level surface closely approximates the minimal gyroid or gyroid minimal surface discovered by Schoen, see Fig. 2.2a. Minimal surfaces have the

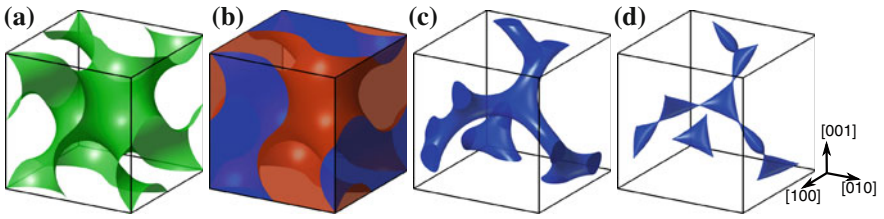

Fig. 2.2 Single-gyroid surfaces calculated using Eq. (2.5). **a** Minimal gyroid surface for $t = 0$. **b** Two helical interpenetrating single-gyroid networks separated by the minimal gyroid surface. **c** Single-gyroid for $t = 1.3$. **d** Pinch-off surface for $t = 1.413$

property that their mean curvature is zero everywhere ($H = 0$) and thus are a subset of CMC surfaces. For this special surface, as mentioned earlier, an analytical expression is known. Using the Enneper-Weierstrass representation, which provides an equation for the coordinates of minimal surfaces, the exact parametrization of the triply periodic gyroid minimal surface can be derived [9].
The minimal gyroid surface divides space into two helical regions or networks, each claiming a volume fraction of 50 %, see Fig. 2.2b. The surface embeds an inversion center which interchanges the two sides of the surface and also the two regions which it partitions. The separated networks are enantiomorphic, which means that one network is left-handed, the other one right-handed [9].

- $0 < |t| \leq 1.413$:
  An increasing $|t|$ is related to a monotonic increase/decrease in the volume of each of the two related networks and leads to an increase in the absolute mean curvature $|H|$, see Fig. 2.2c. Correlated to the change in volume fraction is the growing offset of the surface from the $t = 0$ base surface. For t, the surface on one side of the minimal surface ($t = 0$) with a certain offset, while for $-t$ the surface lies on the opposite side with the same offset. This behavior will become clearer when discussing the double-gyroid.
  For $t = 1.413$, the so-called pinch-off surface is generate, see Fig. 2.2d. Experimentally this IMDS is generated when the voided minority networks are replicated by either chemical vapor or atomic layer deposition techniques [21].
- $1.413 < |t| \leq 1.5$:
  For these t values, the SG surface is no longer connected and will be neglected in the following discussion.
- $|t| > 1.5$:
  The SG disappears, since no point $(x, y, z) \in \mathbb{R}^3$ fulfils Eq. (2.5).

2.4 Double-Gyroid

In 1986, Thomas et al. were the first to discover the double-gyroid IMDS in multiarm star diblock copolymers of poly(isoprene) and poly(styrene), but incorrectly identified the new morphology, lying between the lamellar and cylindrical phase, as the

double diamond [22]. Eight years later, in 1994, two groups independently characterized the IMDS observed in a low molecular diblock copolymer melt and in a diblock copolymer blend correctly as DG with $Ia\bar{3}d$ (No. 230) symmetry [23, 24]. These results suggested a reexamination of the star diblock structure with improved X-ray measurements, which led to a reevaluation to DG [25]. Thereafter, the double-gyroid IMDS has been observed in various diblock copolymers [26, 27], in nanoporous silica films [28], in ABA triblock copolymers [29, 30], and in ABC triblock copolymers where the A and C block have identical volume fractions [31].

The simplest method to construct the DG surface is by generating two SG level surfaces with $0 < t \leq 1.413$,

$$F_{SG}(x, y, z) = \pm t, \tag{2.6}$$

which defines a so-called double level surface. By squaring Eq. (2.6) the (single) level surface equation (see Eq. (2.2)) of the DG can be obtained

$$F_{DG}(x, y, z) = (F_{SG}(x, y, z))^2 = t^2 = t'. \tag{2.7}$$

Another way to derive the DG level surface function would have been to use Eq. (2.3) with $Ia\bar{3}d$ as the generating space group, which delivers the same result [10, 11].

In the interval $0 < t \leq 1.413$ the DG level surface effectively divides space into three embedded continuous subvolumes. This phase which is located between the two SG surfaces, centered on the minimal gyroid surface, forms the so-called matrix phase through which the two networks run. Each one of the three networks is periodic in all three principle directions. The matrix phase volume increases with increasing values of t, and thereby gradually reducing the strut diameters of the two enclosed networks.

The matrix is also called the majority phase, because it takes up about 63–66 % of the volume in DG morphologies formed by diblock polymers, and accordingly the networks together are called the minority phase. An unit cell with cubic symmetry $Ia\bar{3}d$ showing the matrix phase together with the two minority networks is presented in Fig. 2.3a. To illustrate that the two distinct intertwined networks are non-intersecting, an arrangement of four unit cells with the matrix phase removed and the two networks colored blue and red is shown in Fig. 2.3b.

When using porous double-gyroid morphologies for nanotechnology applications by selectively removing either the matrix phase or the two networks, the surface area per bulk volume is an important parameter [32]. The double-gyroid's surface area A thereby depends on the network phase volume fraction ϕ. The two parameters necessary to determine the surface area per unit bulk volume were calculated numerically for the different values of t in the following fashion: The surface area was determined by triangulating the DG surface and then adding the area of the individual triangles up, while the volume of the networks was calculated by subdividing the unit cell in small cubes and then counting the number of cubes enclosed by the surfaces of the networks. Fig. 2.4a shows the almost linear dependence of the volume fraction ϕ of

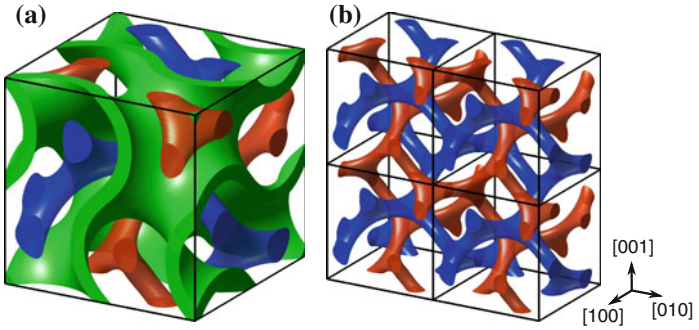

Fig. 2.3 **a** The double-gyroid cubic unit cell showing the matrix phase (*green*) and the two networks (*blue* and *red*). **b** Four cubic unit cells of the double-gyroid network with a volume fraction of 12 % ($t = \pm 1.3$)

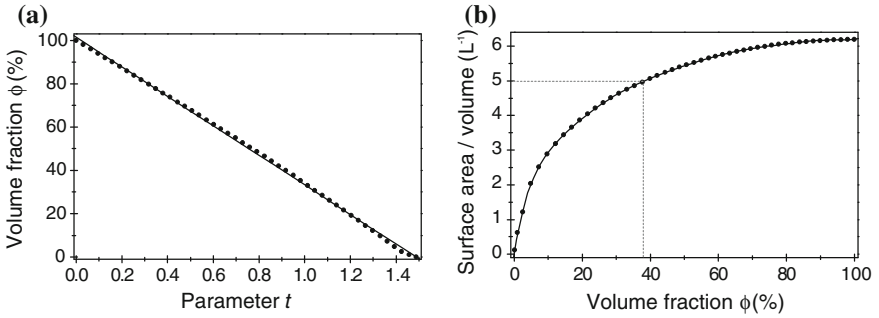

Fig. 2.4 **a** Volume fraction ϕ of the double-gyroid network phase as function of the parameter t fitted with $\phi(t) = 101.5 - 68.1 \cdot t$. **b** Specific surface area to bulk volume ratio of the double-gyroid plotted versus the network phase volume fraction in units of the cubic unit cell dimension L

DG networks on the parameter t. The surface area per unit bulk volume is plotted against the volume fraction of the networks in Fig. 2.4b.

When using structured materials in nanotechnology applications, it is important to know how robust these structures are. The weak points or cleavage planes of a three-dimensional porous structure often coincide with particular two-dimensional cross-sectional planes with a minimal area fraction of the nanostructured material. In order to determine the planes with minimal area fraction of the majority and minority voided double-gyroid networks a MATLAB simulation was used. The simulation numerically calculates the area fraction $A_{\mathrm{hkl}}(d)$ of the 65 % volume percent matrix network parallel to various crystallographic (hkl) planes as a function of the distance d from the point of origin to the intersection point of the plane with the [111] unit cell body diagonal. The results are shown in Fig. 2.5, where $A_{\mathrm{hkl}}(d)$ is plotted against d for the lowest values of $h^2 + k^2 + l^2$. Only for planes parallel to (211) and (110), the area fraction varies significantly around the mean value of 0.65 for different values of d. Whereas the area fraction of the other shown crystallographic planes

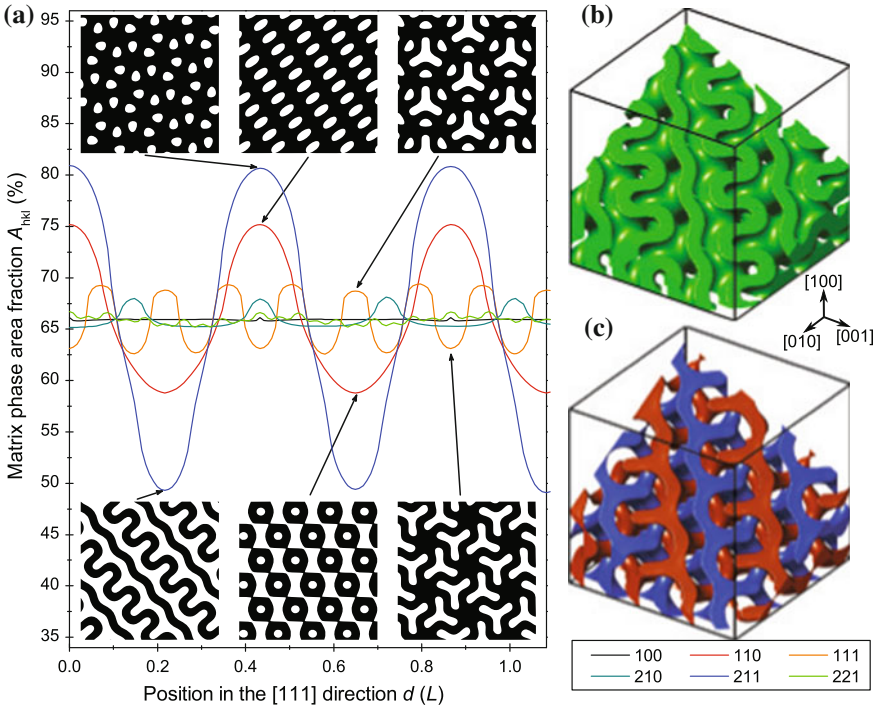

Fig. 2.5 A majority phase volume fraction of 0.65 was used for the presented simulations. **a** The area fraction $A_{\mathrm{hkl}}(d)$ of the matrix phase's cross-sectional cut parallel to various crystallographic hkl planes is plotted against d, where d denotes the distance from the unit cell point of origin to the intersection point of the cross-section with the [111] unit cell body diagonal [33]. The two-dimensional patterns of (110), (111), and (211) plane possessing an extremal area fraction are shown. The matrix phase is colored in black. **b** Matrix and **c** network phase showing the (211) double wave pattern. The frame outlines the volume of 3×3 unit cells

and those with higher $h^2+k^2+l^2$ values hardly depends on d [33]. Thus, especially the cross-sections parallel to the (211) and also the (110) plane with minimal area fraction might serve as predetermined breaking points for double-gyroid majority network structured materials, while the planes with maximal area fraction might act as cleavage planes for minority network structures.

The complex triply periodic branching of gyroidal surfaces defines a fascinating three-dimensional maze. Finding the shortest path connecting two points lying within the maze is interesting from both a theoretical and an experimental point of view. A spherical growth front nucleated at a single site, the starting point, and propagated through this voided double-gyroid maze will find the shortest path to any given end point. Additionally, the propagating growth front will disclose any preferential growth directions through the maze. Experimentally, this can be tested by electroplating an amorphous or highly polycrystalline metal and limiting the number of nucleation sites, see Chap. 6. Since an analytical solution to this problem

seems impossible, here, the results obtained from a computer model simulating the templated and nontemplated growth behavior are presented.

The most convenient approach is to perform the simulations on a cubic lattice, however, this requires a special propagation algorithm that correctly implements the locally spherical growth and avoids preferential growth induced by the nature of the cubic lattice. Here, a modified version of Dijkstra's algorithm, a graph search algorithm that solves the single-source shortest path problem, is employed [34]. For a given starting coordinate, the modified algorithm finds all points that are connected to the starting point by a path with lowest total cost equal to a given total cost C and stores them in a list for the subsequent visualization and analysis. Here, the cost of propagation from one point to a nearest neighbor is defined by their Euclidean distance. The algorithm propagates in the following way:

1. Identify the set of points for the cubic lattice of interest that are accessible to the growing front and mark them as unvisited by assigning a tentative cost value of infinity.
2. Set the starting point as current and its cost to zero.
3. For the current point, consider all of its unvisited neighbors and calculate their tentative cost which is given by the sum of the current point's cost and the cost of propagation from the current point to the considered neighbor. If this cost is less than the previously recorded tentative cost, then overwrite.
4. Add the current point's coordinates to the list meant for later output if its cost equals C.
5. Mark the current point as visited and remove it from the unvisited set.
6. Determine which unvisited point has the lowest cost and set it as the next current point. If the cost does not exceed C, then return to step 3.

Increasing the set of points that are considered as neighbors gives an improved approximation to a spherical growth. However, increasing the distance between the current point and neighbor can lead to omitting a maze obstacle and more time intensive calculations. Here, points lying within a radius of $a\sqrt{11}$ are considered as neighbors, where a is the cubic lattice's repetition length. To test if the model approximates a spherical growth the simulation was run in absence of a maze or scaffold, see Fig. 2.6.

Since the double-gyroid has a cubic unit cell it is sufficient to only consider points with positive coordinates and obtain the full three-dimensional propagation map by mirroring along the coordinate planes. Further, since the two interwoven double-gyroid minority networks share an inversion center that coincides with the unit cell center it is sufficient to restrict the simulation to one network. Both these measures help to reduce the calculation complexity, nevertheless, considering a volume of $7\times7\times7$ gyroid unit cells with a resolution of 60 along each coordinate axis leads to a cubic lattice with a total of 74 million cubes. The results of simulations for a double-gyroid with the voided minority phase having a volume fraction of 12 % are presented in Figs. 2.6 and 2.7.

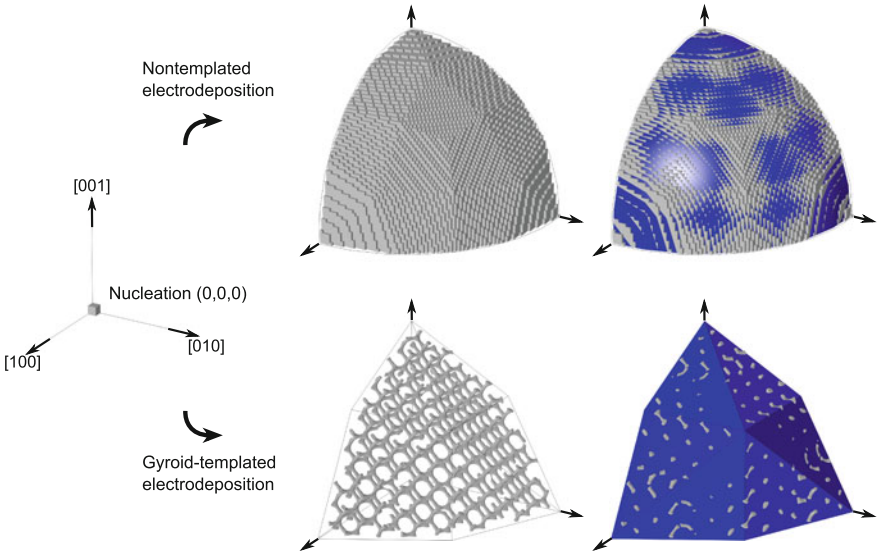

Fig. 2.6 Computer simulation of nontemplated and gyroid-templated amorphous/highly polycrystalline electroplating. In the case of nontemplated deposition a spherical growth front is obtained, as expected. Interestingly, the gyroid-templated simulation reveals preferential growth directions resulting in distinct facets

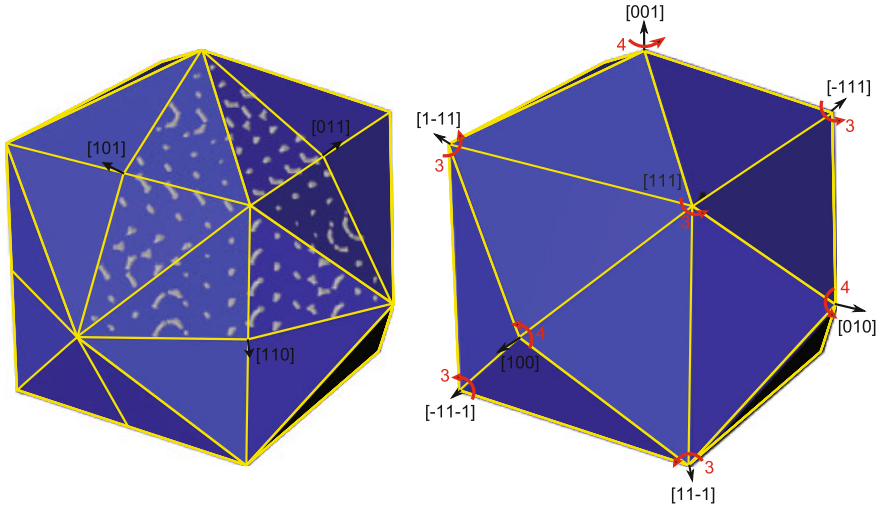

Fig. 2.7 Growth map for a double-gyroid with a volume fraction of 12 %. For this volume fraction the <110> vertices vanish since they lie on a straight line connecting two members of the <111> set. Thus, the <100> and <111> vertices are surrounded by 4 and 6 facets, respectively. The order of rotational symmetry is given in *red*

Preliminary analysis identified the <111> direction to have the fastest growth rate, however, it is still slower than the nontemplated growth. The growth speed shows a local maximum along the <100> directions, while the slowest propagation was found to exist along the <110> direction. The relative growth rate <110>:<100>: <111> is approximately $\sqrt{2}$:$\sqrt{2.5}$:$\sqrt{3}$, which means that the < 110 > vertices lie in very close vicinity of a straight line connecting two members of the <111> set and thus do not appear as such. A comparison of this simulation and one with a gyroidal unit cell rotated by 45° around the z-axis gave the same results, confirming that the obtained results are not an artifact of the propagation algorithm.
Increasing the networks' volume fraction to 35 % changes the relative growth rate <110>:<100>:<111> to approximately $\sqrt{2.4}$:$\sqrt{3}$:$\sqrt{3}$ with the speed in fast directions being identical to nontemplated speed. In this case the <110> directions form vertices, however, they still lie in close vicinity of the straight line connecting two members of the <111> set, making the detection of these vertices and the corresponding facet by means of SEM difficult.

These are only preliminary results, but since the extremal growth directions are identified, simulation restricted to these direction can be performed with a higher accuracy and resolution. Implementing these simulations should be relatively straight-forward and will help to identify the exact growth speed along these directions as a function of the networks' volume fraction. Nevertheless, this computer model suggests that the periodicity of templates with large gyroidal single domains will result in a crystal-like appearance of an electroplated amorphous or highly polycrystalline material. This hypothesis will be tested in Chap. 6.

In summary, the triply periodic double-gyroid IMDS, which generating space group and surface symmetry is $Ia\bar{3}d$ (No. 230), is embedded (free from self-intersection) and has a body centered cubic unit cell with an inversion center. As an IMDS every point on the surface has constant mean curvature. Further, the IMDS divides space into three subvolumes each being continuous, forming two interwinding and enantiomorphic networks, one left-handed, the other one righthanded. Importantly, the three subvolumes are triply periodic and interconnected, which means that on their own they define three-dimensionally self-supporting and freestanding structures. This latter property makes the double-gyroid so interesting as structure for nanotechnology applications.

2.5 Alternating Double-Gyroid

The two interpenetrating networks defining an alternating double-gyroid IMDS posses different volume fractions and as such the IMDS has $I4_132$ symmetry, as discovered in ABC triblock copolymers [31]. However, in the case that the A and C block have identical volume fractions the IMDS has $Ia\bar{3}d$ symmetry, but is still considered to be an alternating double-gyroid since the two networks are made of chemically different materials and the structure as such only has $I4_132$ symmetry. The points (x, y, z) fulfilling Eq. (2.8) define the alternating double-gyroid surface

$$F_{SG}(x, y, z) = \begin{cases} t_1 \\ -t_2 \end{cases}, \tag{2.8}$$

for $t_1 \neq t_2$ and $0 < t_{1,2} \leq 1.413$.

2.6 Core-Shell Double-Gyroid

The core-shell IMDS was first discovered in ABC triblock copolymers where two chemically identical interpenetrating double-gyroid networks are comprised of cores of C encased in shells of B and embedded in a matrix of A [6, 7, 35, 36]. Thus, the core-shell double-gyroid IMDS in these triblock copolymers is pentacontinuous. One could envision, that a copolymer with four or more chemically distinct blocks could also form a version of the core-shell gyroid with more than one shell.

The values of (x, y, z) that solve the following 'quadruple' level surface equation generate the core-shell gyroid surface

$$F_{SG}(x, y, z) = \begin{cases} \pm t_1 \\ \pm t_2 \end{cases}, \tag{2.9}$$

for $t_1 \neq t_2$ and $0 < t_{1,2} \leq 1.413$. The core-shell double-gyroid is a superposition of two double-gyroids with different volume fractions, sharing the same inversion center which results in $Ia\bar{3}d$ symmetry. The symmetry is preserved also when taking the core's and the shell's materials into consideration, since both of their two networks consist out of chemically identical material.

2.7 Gyroid-Like Surfaces

Two more gyroid-like IMDSs were discovered in the phase diagram of copolymers, namely the orthorhombic *Pnna* (No. 52) and the orthorhombic *Fddd* (No. 70) network, see Fig. 2.8. Bailey and colleagues were the first to observe the *Fddd* IMDS in copolymer systems, namely PI-*b*-PS-*b*-PEO. The drawings of the *Fddd* published in [40] suggest a 'core-shell *Fddd*' morphology, while in a later publication [31] an 'alternating *Fddd*' is presented. After the discovery of this noncubic triply periodic morphology in triblock copolymers the orthorhombic *Fddd* was also found to be adopted by diblock copolymers [5, 37]. The *Fddd* IMDS formed by diblock copolymers separates space into two regions that form connected networks which are periodic in three independent directions. Hence, it is considered to be bicontinuous and triply periodic just like the single-gyroid surface.

The first to prove the existence of the orthorhombic *Pnna* IMDS in copolymer melts were Cochran et al. [41]. A triblock copolymer melt was sheared in order

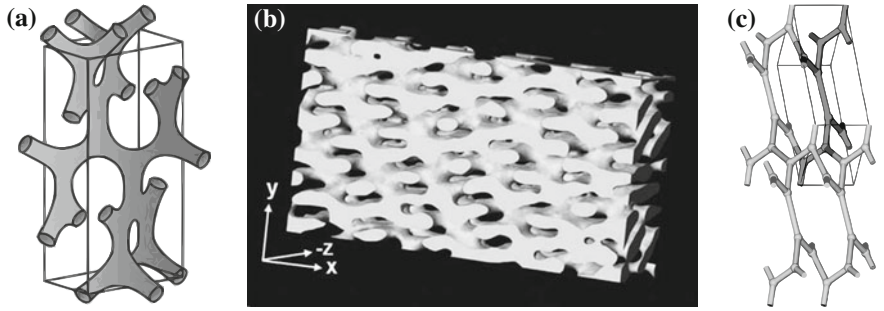

Fig. 2.8 **a** Unit cell of the *Fddd* structure found in diblock copolymers. (Reprinted with permission from Kim et al. [37]. Copyright 2013 American Chemical Society) **b** Reconstructed three-dimensional image of a poly(styrene)-*b*-poly(isoprene) *Fddd* structure obtained by transmission electron microtomography. (Reproduced from Jung et al. [38] with permission of The Royal Society of Chemistry) **c** Ball and stick model of the *Pnna* (No. 52). (Reproduced from Bluemle et al. [39] with permission of The Royal Society of Chemistry)

to induce a network-to-network transition from *Fddd* to *Pnna*. Subsequent to the discovery of the shear-induced *Pnna* morphology, this structure was also found to exist in tetrablock copolymers [39].

References

1. M.R.J. Scherer, Nanostructured Materials via Self-Assembled Templates, University of Konstanz (2009)
2. A.C. Finnefrock, R. Ulrich, A.D. Chesne, C.C. Honeker, K. Schumacher, K.K. Unger, S.M. Gruner, U. Wiesner, Angew. Chem. Int. Ed. **40**(7), 1207–1211 (2001)
3. B.C. Garcia, M. Kamperman, R. Ulrich, A. Jain, S.M. Gruner, U. Wiesner, Chem. Mater. **21**(22), 5397–5405 (2009)
4. G.E.S. Toombes, A.C. Finnefrock, M.W. Tate, R. Ulrich, U. Wiesner, S.M. Gruner, Macromolecules **40**(25), 8974–8982 (2007)
5. M. Takenaka, T. Wakada, S. Akasaka, S. Nishitsuji, K. Saijo, H. Shimizu, M.I. Kim, H. Hasegawa, Macromolecules **40**(13), 4399–4402 (2007)
6. T. Goldacker, V. Abetz, Macromolecules **32**(15), 5165–5167 (1999)
7. T.A. Shefelbine, M.E. Vigild, M.W. Matsen, D.A. Hajduk, M.A. Hillmyer, E.L. Cussler, F.S. Bates, J. Am. Chem. Soc. **121**(37), 8457–8465 (1999)
8. X. Zeng, G. Ungar, M. Imperor-Clerc, Nat. Mater. **4**(7), 562–567 (2005)
9. P.J.F. Gandy, J. Klinowski, Chem. Phys. Lett. **321**(5–6), 363–371 (2000)
10. M. Wohlgemuth, N. Yufa, J. Hoffman, E.L. Thomas, Macromolecules **34**(17), 6083–6089 (2001)
11. H.G. von Schnering, R. Nesper, Z Phys. B Con. Mat. **83**(3), 407–412 (1991)
12. V. Luzzati, P.A. Spegt, Nature **215**(5102), 701–704 (1967)
13. V. Luzzati, A. Tardieu, T. Gulik-Krzywicki, E. Rivas, F. Reiss-Husson, Nature **220**(5166), 485–488 (1968)
14. A.H. Schoen, Infinite periodic minimal surfaces without self-intersections, NASA Technical Note D–5541 (1970).
15. K. Michielsen, D. Stavenga, J.R. Soc, Interface **5**(18), 85–94 (2008)

16. P. Vukusic, J.R. Sambles, Nature **424**(6950), 852–855 (2003)
17. M. Maldovan, A.M. Urbas, N. Yufa, W.C. Carter, E.L. Thomas, Phys. Rev. B **65**(16), 165123 (2002)
18. G. Schröder-Turk, S. Wickham, H. Averdunk, F. Brink, J. Fitz Gerald, L. Poladian, M. Large, S. Hyde, J. Struct. Biol. **174**(2), 290–295 (2011)
19. Z. Almsherqi, F. Margadant, Y. Deng, Interface Focus (2012)
20. Y. Grin, R. Nesper, Z. Krist. **226**(8), 692–710 (2011)
21. J.H. Moon, Y. Xu, Y. Dan, S.-M. Yang, A.T. Johnson, S. Yang, Adv. Mater. **19**(11), 1510–1514 (2007)
22. E.L. Thomas, D.B. Alward, D.J. Kinning, D.C. Martin, D.L. Handlin, L.J. Fetters, Macromolecules **19**(8), 2197–2202 (1986)
23. D.A. Hajduk, P.E. Harper, S.M. Gruner, C.C. Honeker, G. Kim, E.L. Thomas, L.J. Fetters, Macromolecules **27**(15), 4063–4075 (1994)
24. M.F. Schulz, F.S. Bates, K. Almdal, K. Mortensen, Phys. Rev. Lett. **73**(1), 86 (1994)
25. D.A. Hajduk, P.E. Harper, S.M. Gruner, C.C. Honeker, E.L. Thomas, L.J. Fetters, Macromolecules **28**(7), 2570–2573 (1995)
26. G. Floudas, R. Ulrich, U. Wiesner, J. Chem. Phys. **110**(1), 652–663 (1999)
27. S. Ndoni, M.E. Vigild, R.H. Berg, J. Am. Chem. Soc. **125**(44), 13366–13367 (2003)
28. V.N. Urade, T.-C. Wei, M.P. Tate, J.D. Kowalski, H.W. Hillhouse, Chem. Mater. **19**(4), 768–777 (2007)
29. B.J. Dair, C.C. Honeker, D.B. Alward, A. Avgeropoulos, N. Hadjichristidis, L.J. Fetters, M. Capel, E.L. Thomas, Macromolecules **32**(24), 8145–8152 (1999)
30. A. Nykänen, M. Nuopponen, A. Laukkanen, S.-P. Hirvonen, M. Rytelä, O. Turunen, H. Tenhu, R. Mezzenga, O. Ikkala, J. Ruokolainen, Macromolecules **40**(16), 5827–5834 (2007)
31. T.H. Epps, E.W. Cochran, T.S. Bailey, R.S. Waletzko, C.M. Hardy, F.S. Bates, Macromolecules **37**(22), 8325–8341 (2004)
32. C.A. Lambert, L.H. Radzilowski, E.L. Thomas, Philos. Trans. R. Soc. London, Ser. A, **354**(1715), 2009–2023 (1996)
33. T. Hashimoto, Y. Nishikawa, K. Tsutsumi, Macromolecules **40**(4), 1066–1072 (2007)
34. E.W. Dijkstra, Numer. Math. **1**(1), 267–271 (1959)
35. A.J. Meuler, C.J. Ellison, M.A. Hillmyer, F.S. Bates, Macromolecules **41**(17), 6272–6275 (2008)
36. M. Stefik, S. Mahajan, H. Sai, T.H. Epps, F.S. Bates, S.M. Gruner, F.J. DiSalvo, U. Wiesner, Chem. Mater. **21**(22), 5466–5473 (2009)
37. M.I. Kim, T. Wakada, S. Akasaka, S. Nishitsuji, K. Saijo, H. Hasegawa, K. Ito, M. Takenaka, Macromolecules **41**(20), 7667–7670 (2008)
38. J. Jung, H.-W. Park, J. Lee, H. Huang, T. Chang, Y. Rho, M. Ree, H. Sugimori, H. Jinnai, Soft Matter **7**(21), 10424 (2011)
39. M.J. Bluemle, G. Fleury, T.P. Lodge, F.S. Bates, Soft Matter **5**(8), 1587–1590 (2009)
40. T.S. Bailey, C.M. Hardy, T.H. Epps, F.S. Bates, Macromolecules **35**(18), 7007–7017 (2002)
41. E.W. Cochran, F.S. Bates, Phys. Rev. Lett. **93**(8), 087802 (2004)

Springer

http://www.springer.com/978-3-319-00353-5

Double-Gyroid-Structured Functional Materials
Synthesis and Applications
Scherer, M.R.J.
2013, XXI, 198 p., Hardcover
ISBN: 978-3-319-00353-5